

Strength and fracture surface energy of phase-separated glasses

N. MIYATA, H. JINNO

Department of Industrial Chemistry, Faculty of Engineering, Kyoto University, Sakyo-ku, Kyoto 606, Japan

Flexural strength and fracture surface energy were determined for lead borate glasses whose compositions lie in the immiscible region of the $\text{PbO}-\text{B}_2\text{O}_3$ system. The microstructural characterization indicated that the glasses are typical particulate composites which consist of two immiscible phases. For the glasses whose microstructure consists of PbO -rich particles/ B_2O_3 -rich matrix (B_2O_3 -rich side of the miscibility gap), the fracture surface energy was found to decrease with increasing second-phase particles. To explain this behaviour, a crack propagation model in a brittle composite containing "penetrable" particles was proposed. On the other hand, for the glasses whose microstructure consists of B_2O_3 -rich particles/ PbO -rich matrix (PbO -rich side of the miscibility gap), an increase in fracture surface energy with volume fraction of dispersed particles was observed. This phenomenon could be best explained by Lange–Evans theory of fracture in brittle composites containing "impenetrable" particles. It was concluded that, when the critical crack size in a non-dispersed host glass is much larger than the particle size, the crack size in particulate composites is invariant with microstructure and also that the variation of strength results entirely from the variation of fracture toughness.

1. Introduction

It has been suggested that second-phase dispersions in a brittle material can increase fracture surface energy and fracture strength. The increase in fracture surface energy in some brittle particulate composites has been related to the change in crack shape caused by impedance of the crack front by the second-phase obstacles. Lange [1] proposed, based upon a "line tension concept", a mechanism of the momentary pinning of the moving crack front by obstacles, and provided an expression for the fracture surface energy of a brittle particulate composite. Evans [2] elaborated this theory and calculated the line tension contribution to the fracture surface energy as a function of the ratios of the obstacle dimensions and the obstacle spacing, where the obstacles can be considered "impenetrable". He concluded that line tension may be the major contribution to the increase in fracture surface energy of brittle matrix/brittle particle composites. It has been shown, on the

other hand, that an array of non-bonded particles or "soft" particles such as pores can still impede a crack motion, which may lead to an increase in fracture surface energy. Ahlquist [3] and Green *et al.* [4–7] postulated that this effect is a result of localized crack blunting.

However, second-phase dispersions must have a variety of microstructural effects and they can also lower fracture surface energy and strength [8]. General reduction of fracture surface energy by randomly distributed pores in brittle materials is a typical example. Second-phase particles (or pores) can act as stress concentrators in particulate composites when elastic moduli and thermal expansion coefficient of particles are different from those of the matrix. It is then possible that localized stress fields around and within the particles determine the fracture path and aid, in certain circumstances, crack propagation which results in a lowering of the fracture surface energy. The Lange–Evans theory ignores the presence of such stress fields

and failure mechanisms, and hence can not explain the reduction of fracture surface energy by dispersed phases.

It is the purpose of the present investigation, by concentrating upon one particular phase-separated glass system, to gain further understanding of the mechanisms whereby fracture behaviour of brittle materials can be modified by second-phase dispersions.

2. Experimental procedure

2.1. Materials

The samples selected for study were lead borate glasses whose compositions lie in the immiscible region of the $\text{PbO}-\text{B}_2\text{O}_3$ system. This system has one of the best characterized immiscible phase boundaries, which lies between about 1 and 44-wt % PbO [9]. Phase-separation characteristics in this system have been investigated by several authors [9–11]. It has been shown that the microstructures observed at all compositions within the miscibility gap consist essentially of spherical particles of one phase in a continuous matrix of the other phase [10, 11].

The glass samples containing 0 to 45 wt % PbO were prepared. Calculated amounts of PbO and dehydrated B_2O_3 were thoroughly mixed in a mortar. The batches were then melted and stirred in platinum crucibles. To ensure homogeneity, the samples were finely crushed and remelted. After repeating this process two or three times, the samples were cast in stainless steel moulds into both rectangular plates and rectangular bars for each type of measurement. The samples were then heat-treated at temperatures near their annealing points for 30 min.

2.2. Microstructure characterization

Microstructures of fracture surfaces of the samples were determined using replication electron microscopy. Fresh fracture surfaces were etched for 10 sec in 1%HF solutions. The volume fraction and particle diameter of dispersed second-phase in each sample were evaluated for the replica electron micrographs by Fullman's technique [12]. Densities were determined by hydrostatic weighings in kerosene relative to a silica standard. Following theoretical expressions relating the volume fraction of PbO -rich phase to density and composition [10], volume fractions of the PbO -rich phase in the samples were calculated and compared with those evaluated from electron micrographs.

2.3. Strength measurement

Flexural strength was measured using rectangular bars $8\text{ mm} \times 4\text{ mm} \times 40\text{ mm}$. Measurements were made with a testing machine using three-point loading over a 32 mm span. All measurements were made in air at room temperature at a loading rate of 0.5 mm min^{-1} . Six to ten specimens were fractured for each PbO content.

2.4. Fracture toughness and fracture surface energy determinations

2.4.1. Fracture toughness K_{IC}

Fracture toughness values were determined using the three-point bend test of a single-edge-notched beam (SENB) along with the Vickers indentation technique. The latter method has been developed over the last few years based upon a fracture mechanics analysis of the indentation fracture problem [13–17]. The applicability of the indentation technique to fracture toughness evaluation of the present phase-separated glasses has recently been examined by the authors [18]. The indentation method was used to obtain toughness values in the lower PbO composition range in which SENB specimen fabrication is rather laborious and difficult.

2.4.1.1. Three-point bend test. Specimens for the three-point bend test were prepared in the form of rectangular bars $8\text{ mm} \times 4\text{ mm} \times 40\text{ mm}$. One 40 mm edge of each specimen was V-notched with a diamond wheel and a stable sharp crack was induced from the notch by application of a soldering iron tip to the specimen surface just ahead of the notch. Pre-crack lengths were measured by optical microscopy. Specimens were tested in three-point bending over a 32 mm span at a cross-head speed of 0.5 mm min^{-1} . All measurements were carried out in air at room temperature. At least 6 specimens for each PbO content were tested. Fracture toughness values K_{IC} were evaluated from specimen dimensions and fracture load using the equation given by Brown and Srawley [19].

2.4.1.2. Indentation testing. Lawn and Fuller [14] have provided a simple formulation for the well-developed stage of indentation fracture in brittle materials. For the case where the indenter in a contact system is considered to be sharp, the fracture toughness can be related to the contact load and the crack dimension produced as follows:

$$kK_{IC} = P/(\pi^{3/2} \cdot \tan \psi \cdot c^{3/2}), \quad (1)$$

where K_{IC} is the fracture toughness, P is the load, c is the radius of a well-developed median crack, ψ is the half-angle of the indenter (for a Vickers pyramid, $\psi = 74^\circ$, half-angle between opposing pyramid edges), and k is a small correction factor which is introduced by considering some effects associated with contact friction, presence of free surface, etc. in a given specimen/indenter system. Equation 1 has enabled fracture toughness determinations to be made from simple pointed indentation tests.

Specimens about 3 mm thick were used for indentation testing. They were finely polished on one surface in kerosene using alumina abrasives to a $0.3 \mu\text{m}$ finish. Indentation tests were performed using a Vickers diamond pyramid with a microhardness tester at room temperature under a dry N_2 environment. For all the specimens, an indenter load of 1 kg was used. The surface traces of the cracks extending from the impression corners were measured by optical microscopy about 30 min after the load was removed. At least 30 separate indentation patterns were produced on each specimen surface. Using Equation 1, relative toughness values kK_{IC} were evaluated from indenter load and produced crack dimension. Most of the glass samples under study were subjected to both the three-point bend test and the indentation testing. This enabled the correction factor k to be estimated by fitting the indentation data to toughness values obtained from the three-point bending technique. The value of k thus determined made it possible to obtain absolute values of fracture toughness of some samples on which only indentation testing was carried out.

2.4.2. Fracture surface energy

Assuming that conditions of plane strain are met, the effective fracture surface energy Γ is given by the equation [20]

$$\Gamma = \frac{(1 - \nu^2)K_{IC}^2}{2E}, \quad (2)$$

where E is Young's modulus and ν is Poisson's ratio. The elastic properties of the present phase-separated glasses in relation to their microstructure have been studied in detail by Shaw and Uhlmann [21]. Using their published data for Young's modulus and Poisson's ratio, the fracture toughness K_{IC} was converted to the fracture surface energy Γ according to Equation 2.

3. Results

3.1. Microstructural characteristics

As shown by Shaw and Uhlmann [10], the present glasses are composed essentially of spherical particles of one phase in a continuous matrix of the other phase. For the B_2O_3 -rich region (about 1 to 20 wt% PbO) within the miscibility gap, B_2O_3 -rich phase forms a continuous phase, while for the PbO-rich region (about 30 to 44 wt% PbO), the PbO-rich phase is continuous. These particulate microstructures in both regions can be confirmed by replication electron micrographs. Figs 1 and 2 demonstrate fracture surfaces of the samples containing 10 and 40 wt% PbO, respectively. Table I gives the volume fractions of the PbO-rich phase and the dispersed particle sizes determined from lineal analysis of electron micrographs for the compositions studied.

For a binary system which contains a miscibility gap between compositions x_1 and x_2 (weight fraction), the bulk density ρ of the sample and the volume fraction ϕ_2 of the phase of the composition x_2 can be expressed theoretically as [10]



Figure 1 Fracture surface of 10PbO·90B₂O₃ (wt %) sample, showing PbO-rich particles in a B₂O₃-rich matrix. Bar indicates 1 μm .

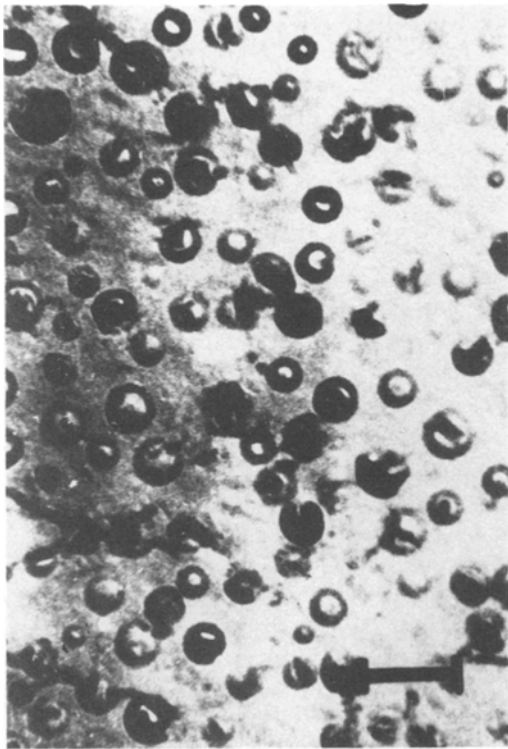


Figure 2 Fracture surface of 40PbO·60B₂O₃ (wt%) sample, showing B₂O₃-rich particles in a PbO-rich matrix. Bar indicates 1 μ m.

$$\rho = \frac{\rho_1 \rho_2}{[(x - x_1)/(x_2 - x_1)](\rho_1 - \rho_2) + \rho_2} \quad (3)$$

and

$$\phi_2 = \frac{\rho_1(x - x_1)}{(x - x_1)(\rho_1 - \rho_2) + (x_2 - x_1)\rho_2}, \quad (4)$$

where ρ_1 and ρ_2 are the densities of the end-member phases. In Fig. 3, the experimentally observed density-composition relation is compared with that predicted from Equation 3. The

TABLE I Structural characteristics of PbO-B₂O₃ glasses

| PbO (wt%) | Volume fraction of PbO-rich phase | Dispersed particle size (μ m) | Microstructure |
|-----------|-----------------------------------|------------------------------------|--|
| 0 | — | — | PbO-rich spherical particles in a B ₂ O ₃ -rich matrix |
| 5 | 0.05 | — | |
| 10 | 0.13 | 0.17 | |
| 13 | 0.18 | 0.18 | |
| 17 | 0.25 | 0.20 | |
| 32 | 0.59 | 0.53 | B ₂ O ₃ -rich spherical particles in a PbO-rich matrix |
| 36 | 0.71 | 0.35 | |
| 40 | 0.84 | 0.40 | |
| 45 | — | — | |

variation of volume fraction of the PbO-rich phase with weight per cent composition is compared in Fig. 4 with the prediction of Equation 4. In both Figs 3 and 4, theoretical curves are established taking the end-member values as $x_1 = 0.01$, $x_2 = 0.44$, $\rho_1 = 1.85$ and $\rho_2 = 3.30$. As Shaw and Uhlmann [10] have already shown for the same glasses, experimental density and volume fraction data are found to agree quite well with the predicted relations on both the B₂O₃-rich and PbO-rich sides of the miscibility gap.

Electron micrographs showed that glass samples having compositions in the central region of the miscibility gap (about 20 to 30 wt% PbO) present some complicating features in microstructure. Because of this, glass compositions in this region were excluded from the present investigation.

3.2. Strength

Fig. 5 shows results of flexural strength measurements. As for glass compositions less than 5 wt% PbO, strength measurements were not carried out because rectangular bar specimens could not be fabricated in a controlled manner. In fact, in this composition range, the viscosity of the melts becomes higher and some difficulties arise in preparing rectangular bar specimens having the dimensions required for the present strength measurements.

It is seen that, in the B₂O₃-rich region, the strength seems to decrease slightly with PbO content, while in the PbO-rich region, a decrease in strength appears clearly with increasing PbO content.

3.3. Fracture surface energy

In Fig. 6, fracture toughness values K_{IC} obtained from the three-point bend test as well as relative toughness values kK_{IC} determined by the Vickers indentation testing are plotted respectively against weight per cent PbO content. For glass samples having 0 to 10 wt% PbO, only Vickers indentation tests were carried out. For the present glasses, as described in our preceding paper [18], relative toughness values kK_{IC} obtained from the Vickers indentation technique were found to be clearly proportional to the toughness values determined by the three-point bend test. The correction factor k involved in the indentation testing can be estimated by fitting the indentation data to toughness values obtained from the three-point bend test. The value for k thus estimated was 0.57 for

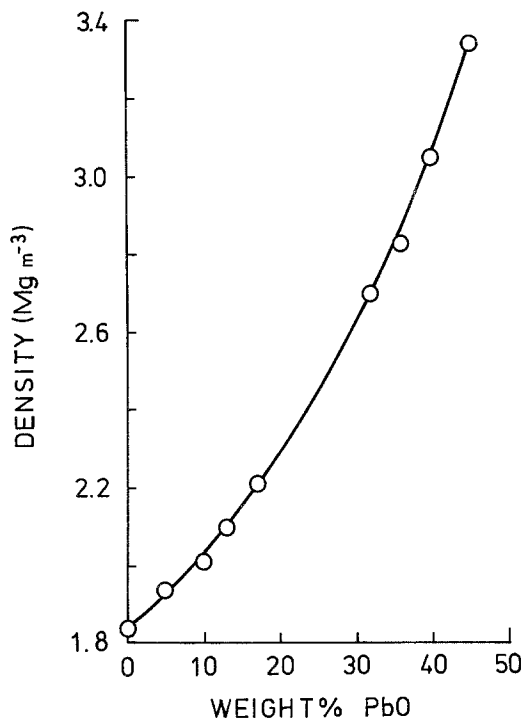


Figure 3 Variation of density with composition over the immiscible region in the system PbO–B₂O₃. Solid curve represents Equation 3.

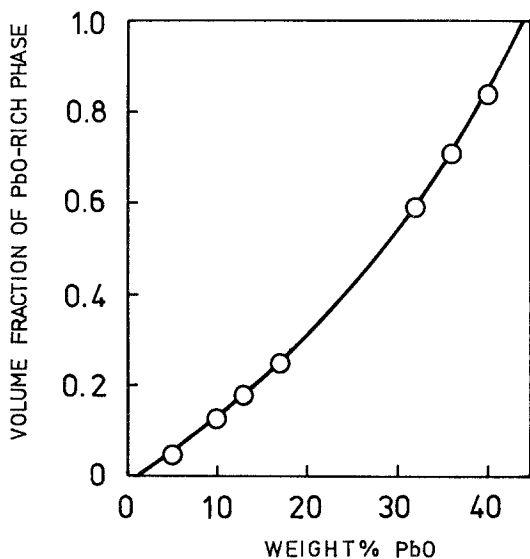


Figure 4 Variation of volume fraction of PbO-rich phase with composition in PbO–B₂O₃ immiscible glasses. Solid curve represents Equation 4.

*In our preceding paper [18], k was estimated at 0.61 by comparing the indentation data with those of the three-point bend test over the entire region of the miscibility gap. Strictly speaking, since the continuous phases in glasses are different from each other on the B₂O₃-rich and PbO-rich sides of the gap, a separate estimation of k should be made for each region.

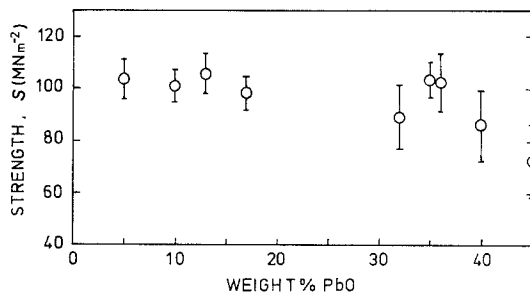


Figure 5 Flexural strength of PbO–B₂O₃ immiscible glasses as a function of wt % PbO.

glasses in the B₂O₃-rich composition range*. Using this estimated value for k , absolute values for fracture toughness were evaluated for glass samples to which the three-point bending technique was not applied. Table II gives the values of fracture toughness, Young's modulus, fracture surface energy and flexural strength. The values for Young's modulus were obtained by interpolation of the Young's modulus data over the miscibility gap published by Shaw and Uhlmann [21]. The values for fracture surface energy were calculated using Equation 2 taking Poisson's ratio as 0.26 for the B₂O₃-rich side and as 0.27 for the PbO-rich side of the miscibility gap [21].

4. Discussion

4.1. Fracture path in the presence of localized stress fields around and within particles

It has been demonstrated that differences in the thermal expansion and the elastic properties of the

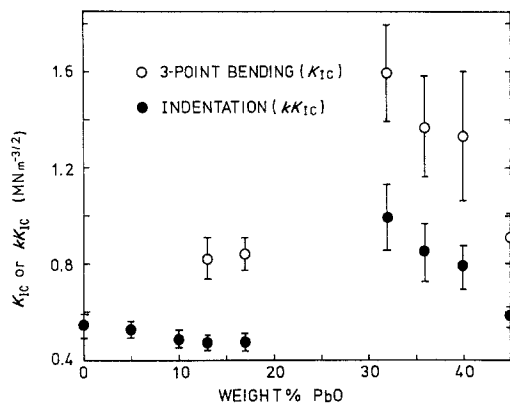


Figure 6 Fracture toughness of PbO–B₂O₃ immiscible glasses as a function of wt % PbO.

TABLE II Mechanical property data for phase-separated PbO–B₂O₃ glasses

| PbO (wt%) | Volume fraction of PbO-rich phase | Fracture toughness $K_{IC}(\text{MNm}^{-3/2})$ | Young's modulus* $E(\text{GPa})$ | Fracture surface energy $\Gamma(\text{Jm}^{-2})$ | Flexural strength $S(\text{MPa})$ |
|-----------|-----------------------------------|--|----------------------------------|--|-----------------------------------|
| 0 | – | 0.954† | 17.3 | 24.5 | – |
| 5 | 0.05 | 0.926† | 18.7 | 21.4 | 104 |
| 10 | 0.13 | 0.856† | 20.2 | 16.9 | 101 |
| 13 | 0.18 | 0.828† | 21.0 | 15.2 | 106 |
| 17 | 0.25 | 0.833† | 22.3 | 14.5 | 98.3 |
| 32 | 0.59 | 1.59 | 31.2 | 37.6 | 89.4 |
| 35 | – | – | 34.5 | – | 104 |
| 36 | 0.71 | 1.38 | 36.2 | 24.4 | 102 |
| 40 | 0.84 | 1.33 | 44.5 | 18.4 | 86.3 |
| 45 | – | 0.906 | 60.4 | 6.30 | 72.6 |

*Data from Shaw and Uhlmann [21]. Each values were obtained by interpolation of their experimental modulus data measured over the miscibility gap.

†Fracture toughness evaluated from Vickers indentation method.

particle and matrix can induce localized stress fields around and within particles. Here, the effect of such stress fields on the fracture path in particulate composites is discussed.

4.1.1. Influence of localized stress fields due to thermal expansion mismatch

A difference in thermal expansion coefficient between particle and matrix causes residual stresses within and around the dispersed particles when the composite cools down from its fabrication temperature. For the case where a spherical particle is embedded in an infinite medium, the stresses in the matrix at a distance r from the centre of the particle are given by [22–24]

$$\sigma_{rr} = -\beta \left(\frac{R}{r}\right)^3 \quad (5)$$

and

$$\sigma_{\theta\theta} = \frac{\beta}{2} \left(\frac{R}{r}\right)^3 \quad (6)$$

with

$$\beta = \frac{(\alpha_m - \alpha_p)\Delta T}{2E_m + \frac{1 - 2\nu_p}{E_p}}, \quad (7)$$

where σ_{rr} and $\sigma_{\theta\theta}$ are radial and tangential stresses, respectively, α is the thermal expansion coefficient, ΔT is the cooling range and R is the particle radius; the subscripts m and p refer to the matrix and particle, respectively. Within the particle, a uniform stress $\sigma = -\beta$ arises. It is then seen from Equations 5 to 7 that, when $\alpha_m < \alpha_p$, the particle is subjected to a tensile stress and the matrix to radial tensile and tangential compressive stresses, and conversely, when $\alpha_m > \alpha_p$, the particle is subjected

to a compressive stress and the matrix to radial compressive and tangential tensile stresses.

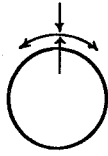
In Fig. 7, the effect of residual thermal stresses on the fracture path in particulate composites is schematically illustrated. As the favoured orientation of the crack path should be that which maximizes the decrease in total system energy [25], the fracture path may also be influenced by the fracture surface energy of each phase, Γ_m and Γ_p . For the case where $\alpha_m > \alpha_p$ local tangential stresses around the particle will cause the radial crack formation during cooling or tend to turn the approaching crack front toward the particle. The crack is, therefore, favoured to intersect the particle. Microcrack formation in the radial direction in the matrix will make it easier for the crack to go through the particle originally in compression. The crack will either go through or circumvent the particle when $\Gamma_p > \Gamma_m$, and will traverse the particle when $\Gamma_p < \Gamma_m$. For the case where $\alpha_p > \alpha_m$ and $\Gamma_p > \Gamma_m$, the local radial tensile stresses around the particle will cause hemispherical microcrack formation during cooling or tend to repel the approaching crack front. The crack is, therefore, favoured to circumvent the particle in this case. For the case where $\alpha_p > \alpha_m$ and $\Gamma_p < \Gamma_m$, however, it is the tensile stresses in the particle which are responsible for microcracking and the crack will go through the particle.

4.1.2. Influence of stress concentrations due to elastic mismatch

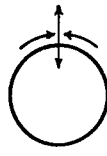
When an external load is applied to a composite, localized stress concentrations are also generated around and within the particles due to a difference

RESIDUAL STRESSES

$$\alpha_m > \alpha_p$$

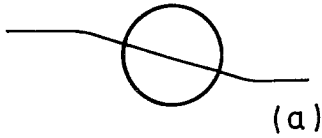


$$\alpha_m < \alpha_p$$

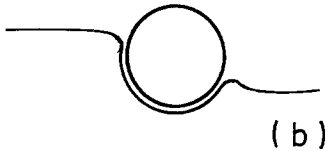
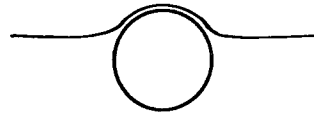


FRACTURE PATH

$$\Gamma_m < \Gamma_p$$



(a)



(b)

$$\Gamma_m > \Gamma_p$$

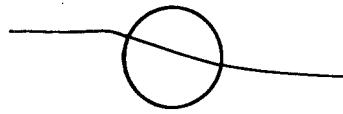
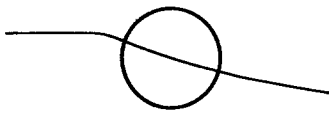


Figure 7 Formation of residual stress fields as a result of thermal expansion mismatch and their effect on fracture path (schematic).

in elastic constants between the particle and matrix. Here, for simplicity, a two-dimensional case of stress concentrations will be considered based upon Goodier's solutions [26] for a cylindrical inclusion in a plate.

Under conditions of uniaxial tensile load, the radial and tangential stresses in the matrix are expressed as

$$\sigma_{rr} = \frac{T}{2}(1 + \cos 2\theta) + 2T \left\{ -A \left(\frac{R}{r} \right)^2 + B \left[3 \left(\frac{R}{r} \right)^4 - 4 \left(\frac{R}{r} \right)^2 \right] \cos 2\theta \right\} \quad (8)$$

$$\sigma_{\theta\theta} = \frac{T}{2}(1 - \cos 2\theta) + 2T \left[A \left(\frac{R}{r} \right)^2 - 3B \left(\frac{R}{r} \right)^4 \cos 2\theta \right] \quad (9)$$

with

$$A = \frac{(1 - 2\nu_p)\mu_m - (1 - 2\nu_m)\mu_p}{4[(1 - 2\nu_p)\mu_m + \mu_p]} \quad (10)$$

and

$$B = \frac{\mu_m - \mu_p}{4[\mu_m + (3 - 4\nu_m)\mu_p]} \quad (11)$$

where T is the applied tensile load, θ is the angle between the tensile direction and the line joining

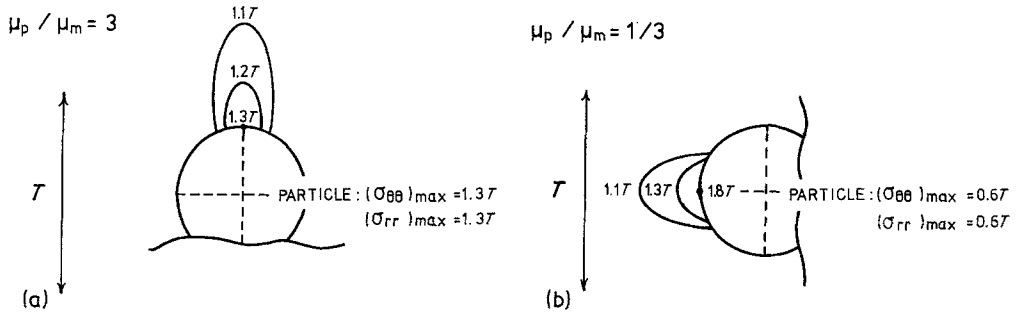


Figure 8 Stress concentration due to the presence of a cylindrical particle (a) stress concentration around and within a particle ($\mu_p/\mu_m = 3$). Radial tensile stress concentration occurs in the matrix in the direction of applied stress and (b) tangential tensile stress concentration around a particle ($\mu_p/\mu_m = 1/3$).

the centre of the inclusion and the point in question, μ_m and μ_p are the rigidity moduli for the matrix and inclusion, respectively. The stresses within the inclusion are given by

$$\text{and} \quad \sigma_{rr} = T(F + G \cos 2\theta) \quad (12)$$

$$\text{with} \quad \sigma_{\theta\theta} = T(F - G \cos 2\theta) \quad (13)$$

$$F = \frac{(1 - \nu_m)\mu_p}{(1 - 2\nu_p)\mu_m + \mu_p} \quad (14)$$

$$\text{and} \quad G = \frac{2(1 - \nu_m)\mu_p}{\mu_m + (3 - 4\nu_m)\mu_p}. \quad (15)$$

It should be noted that the quantities A and B are always similar in magnitude over the range of Poisson's ratios of commonly used materials. The same is true for the quantities F and G .

In the case of a high modulus inclusion ($\mu_p > \mu_m$), the stress concentrations arise around and within the inclusion. The radial tensile stress concentration occurs in the matrix in the orientation $\theta = 0^\circ$. On the other hand, in the case of a low modulus inclusion ($\mu_p < \mu_m$), the tangential tensile stress concentration occurs in the matrix in the orientation $\theta = 90^\circ$. In Fig. 8 stress concentration contours predicted from Equations 8 to 15 are illustrated for (a) $\mu_p/\mu_m = 3$ and (b) $\mu_p/\mu_m = 1/3$. It is assumed that Poisson's ratio for each phase takes equally the value 0.25. As seen from these examples, the regions of significant stress magnification are very localized.

The localized stress fields due to elastic mismatch can induce microcracks associated with the particles during stressing of composites. They can also alter the orientation of a propagating primary crack. Fig. 9 illustrates schematically possible fracture paths which result from the differences in the elastic moduli and the fracture surface energies of the particle and matrix. The

crack will either go through or circumvent the particle, depending upon the differential fracture surface energy. For real particulate composites, stress concentrations due to elastic mismatch must be superimposed on the residual thermal stresses discussed in the preceding section.

4.2. Interpretation of experimental results

4.2.1. Properties of the end-member phases

Table III shows some mechanical properties for the end-member phases, estimated by interpolation of the experimental data listed in Table II. Table III also includes thermal expansion coefficient data compiled by Takamori [27]. It is seen that one of the end-member phases, 1 wt % PbO glass, has lower Young's modulus, higher fracture surface energy and higher thermal expansion coefficient than the other end-member phase, 44 wt % PbO glass.

4.2.2. Glasses consisting of PbO-rich particles in a B_2O_3 -rich matrix

For glass compositions on the B_2O_3 -rich side within the miscibility gap, the fracture path is expected to go through the particles as shown schematically in Fig. 10a. Therefore, the Lange-Evans theory is inapplicable to the present case.

Let us now consider the contribution of second-phase particles to the fracture surface energy when the particles are considered "penetrable". If it is assumed that the crack will simply pass through the average area of each phase, stereological considerations lead to the following expression for the fracture surface energy of composites

$$\begin{aligned} \Gamma &= (1 - \phi)\Gamma_m + \phi\Gamma_p \\ &= \Gamma_m - (\Gamma_m - \Gamma_p)\phi, \end{aligned} \quad (16)$$

where ϕ is the volume fraction of the dispersed

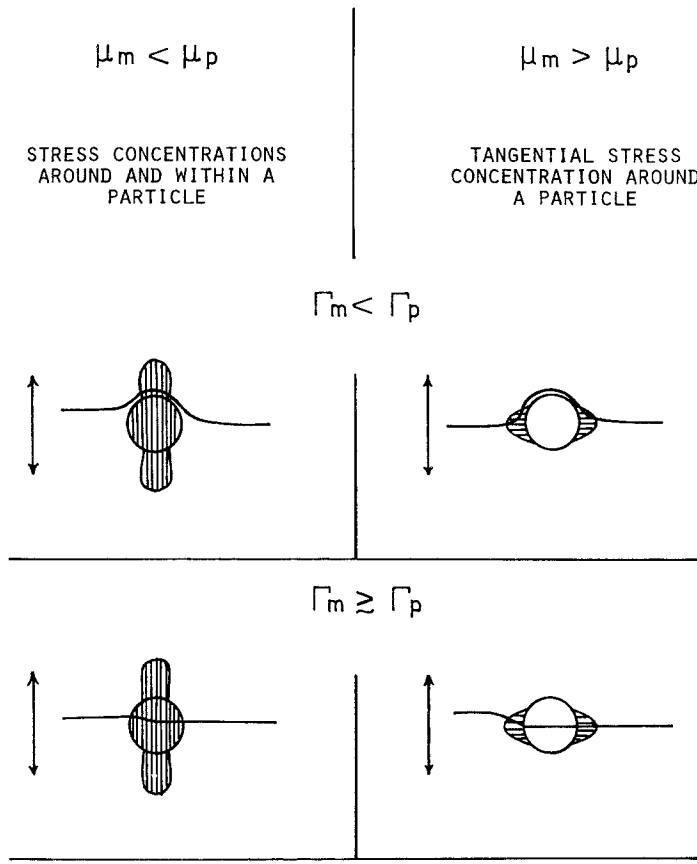


Figure 9 Possible fracture paths resulting from the elastic mismatch in particulate composites (schematic). Arrows indicate the direction of applied tensile load; shaded areas are stress-concentrated regions present prior to fracture.

second-phase. However, it is unlikely that the crack passes through the stereological average areas of the two phases. It can be assumed that the crack will seek the path having a minimum area of matrix with a higher fracture surface energy than the particles. That is, the crack will suffer local deviations from its main plane, seeking preferentially the nearest-neighbour distances between particles. If this crack propagation mechanism occurs, the volume fraction of dispersed phase ϕ in Equation 16 should be replaced by a local volume fraction of dispersed particles ϕ_1 which is defined as

$$\phi_1 = (\bar{L}_3/\Delta_3)^3, \quad (17)$$

where \bar{L}_3 is the mean intercept length of randomly

distributed particles and Δ_3 is the average distance between nearest-neighbour pairs of particles in a particular volume. For a dilute dispersion of randomly distributed spherical particles of diameter D , the nearest-neighbour distance in a volume is approximated as [28]

$$\Delta_3 \approx 0.554(\pi D^2 \lambda / 4)^{1/3}, \quad (18)$$

where λ is the mean free distance between particles. The quantity λ can be approximated as $2D/(3\phi)$ for small volume fractions of dispersed spheres [12]. Then Δ_3 can be written as

$$\Delta_3 \approx 0.447D/\phi^{1/3}. \quad (19)$$

On the other hand, \bar{L}_3 is given by $2D/3$ for ran-

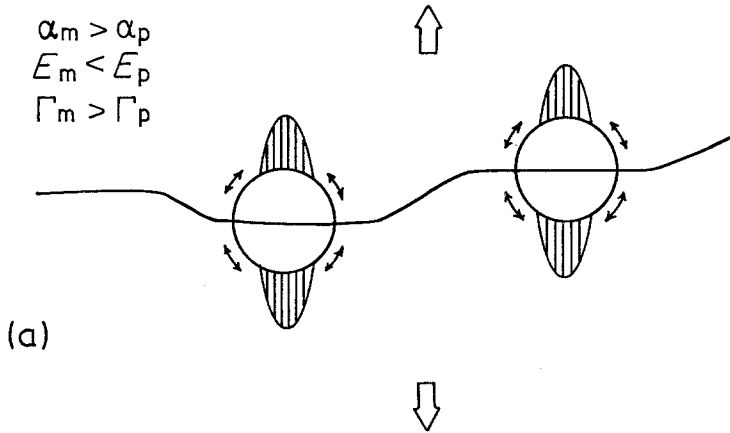
TABLE III Estimated mechanical data for the end-member phases

| End-member phase | Fracture toughness $K_{IC}(\text{MNm}^{-3/2})$ | Young's modulus* $E(\text{GPa})$ | Poisson's ratio* ν | Fracture surface energy $\Gamma(\text{Jm}^{-2})$ | Thermal expansion coefficient† $\alpha(10^{-6} \text{ } ^\circ\text{C}^{-1})$ |
|-------------------|---|-------------------------------------|---------------------------|---|--|
| 1 wt % PbO glass | 0.947 | 17.5 | 0.26 | 23.9 | ~ 14 |
| 44 wt % PbO glass | 0.960 | 56.5 | 0.27 | 7.56 | ~ 7 |

*After Shaw and Uhlmann [21].

†After Takamori [27].

PbO-RICH PARTICLES / B₂O₃-RICH MATRIX



B₂O₃-RICH PARTICLES / PbO-RICH MATRIX

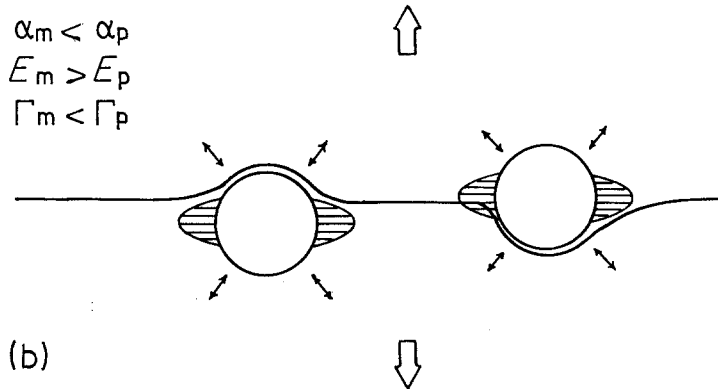


Figure 10 Schematic of fracture path expected for (a) glasses consisting of PbO-rich particles/B₂O₃-rich matrix, and (b) glasses consisting of B₂O₃-rich particles/PbO-rich matrix. Arrows around each particle represent residual thermal tensile stresses in the matrix. Shaded areas represent stress-concentrated regions in the matrix produced by the elastic mismatch.

domly dispersed spheres [12]. Hence it follows from Equation 17

$$\phi_1 = (\bar{L}_3/\Delta_3)^3 = 3.33\phi \quad (20)$$

and the fracture surface energy is given by

$$\begin{aligned} \Gamma &= (1 - \phi_1)\Gamma_m + \phi_1\Gamma_p \\ &= \Gamma_m - (\Gamma_m - \Gamma_p)\phi_1 \\ &= \Gamma_m - 3.33(\Gamma_m - \Gamma_p)\phi. \end{aligned} \quad (21)$$

In Fig. 11, the reduced fracture surface energies obtained for the glasses consisting of PbO-rich particles/B₂O₃-rich matrix are plotted against the volume fraction of dispersed particles. The theoretical prediction from Equation 21 is represented by a solid line, established by taking the values as $\Gamma_m = 23.9 \text{ Jm}^{-2}$ and $\Gamma_p = 7.56 \text{ Jm}^{-2}$. For comparison, Equation 16 is also represented in the figure by a broken line. As expected, the experimental

data agree quite well with the theoretical prediction over the volume fraction range lower than 0.15. The observed deviations in the volume fraction range higher than 0.15 can be attributed to the fact that Equation 18 or 19 is no longer valid for larger volume fractions of dispersed particles.

The size of the critical crack from which catastrophic failure initiates can be estimated with knowledge of the strength and fracture toughness. By arranging Griffith's fracture equation, the critical crack size can be expressed as [29]

$$a = \frac{Y^2 K_{IC}^2}{2S^2}, \quad (22)$$

where a is the crack depth in the surface, S is the fracture stress and Y is a constant which depends on the crack and specimen geometry ($Y = 1.12$ for a surface half-penny crack [29]). Assuming that failure is initiated from a penny-shaped surface

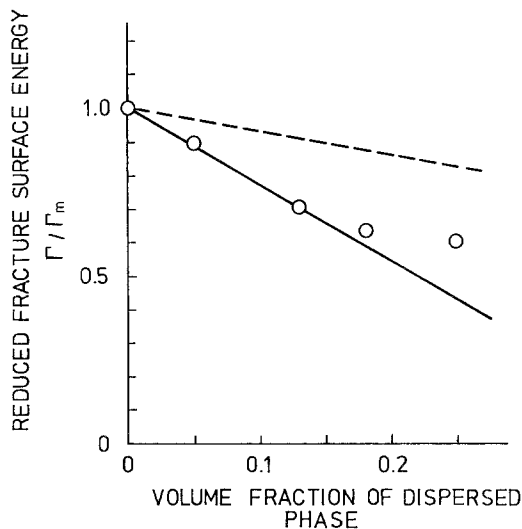


Figure 11 Reduced fracture surface energy for glasses consisting of PbO-rich particles/B₂O₃-rich matrix plotted against the volume fraction of dispersed particles. Solid line represents Equation 21 and broken line, Equation 16.

crack and using the values of fracture toughness and flexural strength listed in Table II, the critical crack sizes are calculated from Equation 22 for the glasses under consideration. The results are shown in Table IV. This table suggests that the present dispersed fine particles being considered “penetrable” have no effect on the critical crack size, although they can influence the fracture surface energies. Thus, the strength and fracture toughness in the present type of composites vary in parallel with volume fraction of dispersed particles under the same testing conditions.

4.2.3. Glasses consisting of B₂O₃-rich particles in a PbO-rich matrix

As shown in Fig. 10b, the fracture path in these two-phase composites is considered to circumvent the particles. It is then expected that the observed increase in fracture surface energy with increasing second-phase particles can be explained by the application of the Lange–Evans theory [1, 2].

TABLE IV Calculated critical crack size for glasses consisting of PbO-rich particles/B₂O₃-rich matrix

| PbO (wt %) | Volume fraction of dispersed phase | Dispersed particle size $D(\mu\text{m})$ | Calculated critical crack size $a(\mu\text{m})$ |
|------------|------------------------------------|--|---|
| 5 | 0.05 | — | 50 |
| 10 | 0.13 | 0.17 | 45 |
| 13 | 0.18 | 0.18 | 38 |
| 17 | 0.25 | 0.20 | 45 |

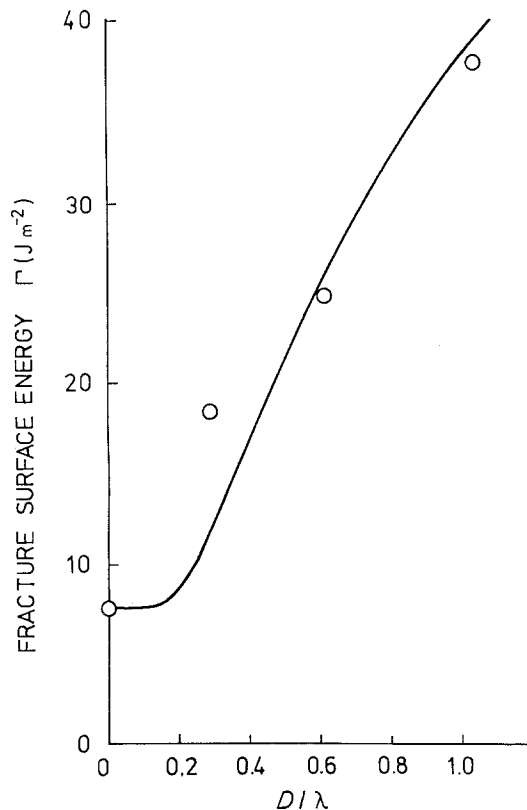


Figure 12 Fracture surface energy for glasses consisting of B₂O₃-rich particles/PbO-rich matrix as a function of the ratio of the particle size to the particle spacing, D/λ . Solid curve represents the line tension contribution calculated from Evans' theory [2].

Lange [1] found that the fracture surface energy is linearly related to the reciprocal of the mean free path between dispersed particles

$$\Gamma = \Gamma_m + \frac{\tau}{\lambda}, \quad (23)$$

where τ is the line tension of the crack front. Evans [2] elaborated Lange's theory and calculated the line tension contribution to the fracture surface energy assuming “impenetrable” particles. In Fig. 12, the fracture surface energies for glasses consisting of B₂O₃-rich particles/PbO-rich matrix are plotted against the ratio of the particle size to the particle spacing, D/λ where $\lambda = 2D(1 - \phi)/(3\phi)$ for randomly dispersed spherical particles [12]. The theoretical line tension contribution calculated from Evan's theory is drawn in Fig. 12 by a solid curve. It is found that the measured fracture surface energy varies with D/λ in a similar manner to the predicted line tension contribution. This indicates that the second-phase particles act as “impenetrable” obstacles and the line tension

TABLE V Calculated critical crack size for glasses consisting of B₂O₃-rich particles/PbO-rich matrix

| PbO (wt %) | Volume fraction of dispersed phase | Dispersed particle size D (μm) | Calculated critical crack size a (μm) |
|------------|------------------------------------|--------------------------------|---------------------------------------|
| 45* | — | — | 98 |
| 40 | 0.16 | 0.40 | 149 |
| 36 | 0.29 | 0.35 | 114 |
| 32 | 0.41 | 0.53 | 198 |

*Homogeneous glass composition which lies just outside the miscibility gap.

may be the major contribution to the increase in the fracture surface energy with second-phase particles.

The critical crack sizes for the present two-phase glasses were calculated in a similar manner to the preceding section and the results are listed in Table V. Taking into account the fact that a large amount of scatter must be necessarily included in each of the calculated crack sizes, the critical crack size should be regarded invariant with volume fraction of dispersed B₂O₃-rich particles. The dispersed particle size is found to be much smaller than the crack size in the homogeneous glass, and the impenetrable second-phase dispersion appears to have no effect on the crack size. This suggests that the crack size in particulate composites is invariant with their microstructure regardless of the "particle impenetrability", when the critical crack size in the host glass without a dispersed phase is much larger than the particle size. The crack size will be related to the composite microstructure only when the particle size is comparable to the average crack size in the host glass. It is then concluded that the critical crack size in the present glasses remains constant as long as the testing condition is identical, and observed increases in strength result entirely from increases in fracture toughness.

5. Summary

The present study was concerned with the fracture behaviour of two-phase brittle matrix/brittle particle composites. Flexural strength, fracture toughness and fracture surface energy were measured for lead borate glasses whose compositions lie in the immiscible region of the PbO—B₂O₃ system. The microstructural characterization indicated that the glasses under study were typical particulate composites consisting of two immiscible phases, B₂O₃-rich and PbO-rich phases. The microstructure

consists of PbO-rich particles/B₂O₃-rich matrix for glass compositions on the B₂O₃-rich side of the miscibility gap, and conversely B₂O₃-rich particles/PbO-rich matrix for glass compositions on the PbO-rich side of the gap.

After discussing localized stress fields generated around and within particles due to elastic and thermal expansion mismatch and their effects on the fracture path in brittle composites, mechanical data obtained for the present two types of particulate composites were interpreted in terms of the properties and amount of each phase and the microstructural effects. An expression was formulated for the fracture surface energy of a brittle composite containing "penetrable" particles. This expression could well explain the decrease in fracture surface energy with increasing second-phase particles observed for the composite system consisting of PbO-rich particles/B₂O₃-rich matrix. On the other hand, the Lange—Evans theory explained well the observed increase in fracture surface energy for the composite system consisting of B₂O₃-rich particles/PbO-rich matrix, in which particles can be considered "impenetrable".

It was concluded that, when the critical crack size in the non-dispersed host glass is much larger than the particle size, the crack size in particulate composites is invariant with microstructure regardless of the "particle impenetrability", and that the strength is controlled by the fracture toughness, i.e. the resistance of the material to crack propagation.

Acknowledgements

Grateful acknowledgement is made to Mr K. Tomita, Mr M. Nabae and Mr T. Shiogai for their assistance in the experimental work. The authors also wish to express their appreciation to Professor M. Tashiro of Kyoto University for his kind co-operation in preparing the electron micrographs.

References

1. F. F. LANGE, *Phil. Mag.* **22** (1970) 983.
2. A. G. EVANS, *ibid.* **26** (1972) 1327.
3. C. N. AHLQUIST, *Acta Met.* **23** (1975) 239.
4. D. J. GREEN, P. S. NICHOLSON and J. D. EMBURY, *J. Mater. Sci.* **12** (1977) 987.
5. D. J. GREEN, P. S. NICHOLSON, "Fracture Mechanics of Ceramics", Vol. 4 edited by R. C. Bradt, D. P. H. Hasselman and F. F. Lange (Plenum Press, New York, 1978) p. 945.
6. D. J. GREEN, P. S. NICHOLSON and J. D. EMBURY, *J. Mater. Sci.* **14** (1979) 1413.

7. *Idem, ibid.* **14** (1979) 1657.
8. R. W. RICE, "Treatise on Materials Science and Technology", Vol. 11 edited by R. K. MacCrone (Academic Press, New York, 1977) p. 234.
9. J. ZARZYCKI and F. NAUDIN, *Phys. Chem. Glasses* **8** (1967) 11.
10. R. R. SHAW and D. R. UHLMANN, *J. Non-Cryst. Sol.* **1** (1969) 474.
11. R. R. SHAW and J. F. BREEDIS, *J. Amer. Ceram. Soc.* **55** (1972) 422.
12. R. L. FULLMAN, *Trans. AIME* **197** (1953) 447.
13. B. R. LAWN and M. V. SWAIN, *J. Mater. Sci.* **10** (1975) 113.
14. B. R. LAWN and E. R. FULLER, *ibid.* **10** (1975) 2016.
15. A. G. EVANS and T. R. WILSHAW, *Acta Met.* **24** (1976) 939.
16. A. G. EVANS and E. A. CHARLES, *J. Amer. Ceram. Soc.* **59** (1976) 371.
17. M. V. SWAIN, J. T. HAGAN and J. E. FIELD, *J. Mater. Sci.* **12** (1977) 1914.
18. N. MIYATA and H. JINNO, *J. Non-Cryst. Sol.* **38/39** (1980) 391.
19. W. F. BROWN, Jr and J. E. SRAWLEY, "Plane Strain Crack Toughness Testing of High Strength Metallic Materials", ASTM STP 410 (ASTM, Philadelphia, 1966).
20. A. S. TETELMAN and A. J. McEVILY, Jr, "Fracture of Structural Materials" (John Wiley and Sons, New York, 1967).
21. R. R. SHAW and D. R. UHLMANN, *J. Non-Cryst. Sol.* **5** (1971) 237.
22. G. M. SMITH, *J. Amer. Concrete Inst.* **27** (1956) 791.
23. D. WEYL, *Ber. Deut. Keram. Ges.* **36** (1959) 319.
24. J. SELSING, *J. Amer. Ceram. Soc.* **44** (1961) 419.
25. B. R. LAWN and T. R. WILSHAW, "Fracture of Brittle Solids" (Cambridge University Press, Cambridge, 1975) p. 66.
26. J. N. GOODIER, *J. Appl. Mech.* **1** (1933) 39.
27. T. TAKAMORI, "Treatise on Materials Science and Technology", Vol. 17 edited by M. Tomozawa and R. H. Doremus (Academic Press, New York, 1979) p. 173.
28. E. E. UNDERWOOD, "Quantitative Stereology" (Addison-Wesley, Reading, Massachusetts, 1970) p. 80.
29. J. J. MECHOLSKY, S. W. FREIMAN and R. W. RICE, *J. Mater. Sci.* **11** (1976) 1310.

Received 25 November 1980 and accepted 2 February 1981.